



Deciphering the ocean bottom pressure variation in the Logatchev hydrothermal field at the eastern flank of the Mid-Atlantic Ridge

Hans-Hermann Gennerich and Heinrich Villinger

Department of Geosciences, University of Bremen, Klagenfurter Strasse, D-28359 Bremen, Germany
(hherm@uni-bremen.de)

[1] Ocean bottom pressure data from the Logatchev hydrothermal field (LHF) are presented and analyzed. The data were collected with two ocean bottom pressure meters (OBPs), constructed at the University of Bremen, that are capable of recording signals with frequencies up to 0.25 Hz. Over the long-term, a nearly 2.5 kPa (25 cm water column equivalent) pressure variation over 3.7 years is observed, which is consistent with uplift followed by subsidence, but cannot unequivocally be discerned from instrumental drift. Medium-term pressure variations are compared with satellite surface topography, satellite gravity, ocean modeling, and in situ data from an OBP 700 km away. It is shown that fluctuations in the oceanic mass distribution dominate the variations in this frequency range and that oceanic modeling and data from a 700 km distant OBP are positively correlated with the LHF bottom pressure time series. The short-term variations are dominated by microseisms originating from sea surface waves and pressure waves from earthquakes as can be shown by comparison with weather buoy and teleseismic data.

Components: 10,100 words, 20 figures, 2 tables.

Keywords: Logatchev hydrothermal field; Mid-Atlantic Ridge; gravity waves; ocean bottom pressure; seafloor deformation; surface waves.

Index Terms: 1209 Geodesy and Gravity: Tectonic deformation (6924); 3017 Marine Geology and Geophysics: Hydrothermal systems (0450, 1034, 3616, 4832, 8135, 8424); 3075 Marine Geology and Geophysics: Submarine tectonics and volcanism.

Received 18 November 2010; **Revised** 16 May 2011; **Accepted** 16 May 2011; **Published** 9 July 2011.

Gennerich, H.-H., and H. Villinger (2011), Deciphering the ocean bottom pressure variation in the Logatchev hydrothermal field at the eastern flank of the Mid-Atlantic Ridge, *Geochem. Geophys. Geosyst.*, 12, Q0AE03, doi:10.1029/2010GC003441.

Theme: From the Mantle to the Ocean: Life, Energy, and Material Cycles at Slow Spreading Ridges

Guest Editors: C. Devey, N. Dublilier, J. Lin, N. Le Bris, and D. Connelly

1. Introduction

[2] Monitoring of magmatic and hydrothermal activity on land has a long history with well-established and mature technologies and sophisticated data analysis methods [Decker, 1986].

Phenomena such as surface uplift, subsidence or tilt; variations in tremor or microseismic activity; sudden changes in temperature, volume or character of hydrothermal springs; and emanations of gases or ash may be precursors used in warning systems in volcanically active areas. Measurement of these parameters can either be done by installing a sensor



network or with remote methods such as airborne and satellite observations. Magmatic systems on the seafloor produce, in principle, the same phenomena as those on land; however, it is much more difficult to measure them. As the seafloor lies below highly conductive seawater, remote observations are limited to acoustic methods. Instruments have to work completely autonomously and have internal power supplies. In addition, real-time access to data is generally not possible, although this will probably change in the future with seafloor networks like Neptune (<http://www.neptunecanada.ca>).

[3] Series of small earthquakes and tremors accompany magmatic dyke injections [Dziak and Fox, 1999; Dziak *et al.*, 1995; Fox *et al.*, 1995] which initiate extensional processes, subsidence and normal faulting at the mid-ocean ridges (MOR) [Carbotte *et al.*, 2006; Chadwick and Embley, 1998; Rubin and Pollard, 1988]. Seafloor vibrations caused by earthquakes or tremors emanate pressure waves into the overlying water column called tertiary waves (T waves) [Williams *et al.*, 2006]. Uplift and subsidence of the seafloor express themselves as pressure variations at the seafloor. The basic principle is that if the seafloor rises, the overlying water column gets thinner and the water pressure at the seafloor decays; conversely, the pressure increases if the seafloor subsides. Tremors, earthquakes and seafloor deformations have in common that they can be identified through pressure variations in the water column at the seafloor. Consequently, monitoring the water pressure variations at the seafloor captures a variety of indicators of changes in the hydrothermal system. An ocean bottom pressure meter (OBP) is a well-suited tool to measure these variations.

[4] In a few previous studies the variation of the seafloor elevation at the Axial Seamount (Juan de Fuca ridge) was surveyed since 1987 with a stationary OBP which revealed volcanic uplift and subsidence in the range of 10–20 cm/a and one event with 3 m subsidence in the central caldera [Fox, 1990, 1993, 1999]. Since 2000, differential measurements by campaign-style visiting of installed benchmarks at the seafloor supplemented the continuous monitoring [Chadwick *et al.*, 2006; Nooner and Chadwick, 2009]. Similar deformation rates of approximately 10 cm/a were found through campaign-style measurements at the Kilauea (Hawaii, United States) [Phillips *et al.*, 2008] and by Fujimoto *et al.* [2003] in a cross section across the East Pacific Rise at 18°25.6'S with an array of three bottom pressure gauges overlain by an El Niño signal in all their OBPs records. At the Lucky Strike Volcano (MAR, 37°N) a campaign-style OBP survey is in

progress [Ballu *et al.*, 2009]. OBP data from the TAG field at the Mid-Atlantic Ridge (MAR, 26°N) revealed periodic pressure variations with spectral peaks between 22 min and 53 min and an amplitude of up to 13 mm water column equivalent (wce) which were interpreted as being caused by shallow subsurface pore pressure variations resulting in seafloor deformation [Sohn *et al.*, 2009].

[5] The detection threshold of the teleseismic network for earthquakes in the oceans is typically at magnitudes of $m_b > 4$ [Dziak *et al.*, 2007]. Earthquakes generated at MORs are relatively weak and are mostly missed by global seismic networks. Local arrays of ocean bottom seismometers (OBSs) and hydrophones [Fox *et al.*, 1995], which have significantly higher sensitivity than the distant teleseismic networks on land, are needed to monitor these events such as the horizontal migration of earthquake swarms as a trace of intruding dykes [Dziak *et al.*, 2007].

[6] Volcanic and hydrothermal tremor [Chouet, 1985; Konstantinou and Schlindwein, 2002] lasting minutes to months radiates at frequency peaks in a wide band down to very low frequencies of 0.02 Hz [Chouet, 2003; Pozgay *et al.*, 2005]. Submarine tremors were detected with the help of hydrophones [Dziak *et al.*, 2002, 2004; Fox *et al.*, 1995; Sohn *et al.*, 1995] and high-frequency OBSs [Monigle, 2009] at the MAR, the East Pacific Rise and the Juan de Fuca Ridge. Signals which are not originated by magmatic, tectonic or hydrothermal activity and which might be also observed by the OBP are caused by mass variations within the ocean [Watts *et al.*, 2001] and by waves at the sea surface [Kedar *et al.*, 2008].

[7] The OBP data presented here were collected in the framework of a multidisciplinary study to investigate time scales of activities in the Logatchev hydrothermal field (LHF). The local geological setting of the LHF site was described by Petersen *et al.* [2009]. The area is located on a terrace at the eastern flanks of the MAR at 14°45'N 44°59'W about 3000 m below sea level (Figure 1). Strongly rotated fault blocks [Smith *et al.*, 2008] indicate a high degree of extensional tectonic activity in an area with a high degree of low-level seismicity [Escartín *et al.*, 2003; Smith *et al.*, 2008]. The observed absence of $m_b > 4$ events is typical for hydrothermally active regions at the MAR [Mazarovich and Sokolov, 2002]. The question of how seafloor deformation is associated with the hydrothermal activity in the LHF is largely unknown. We have made a joint approach to

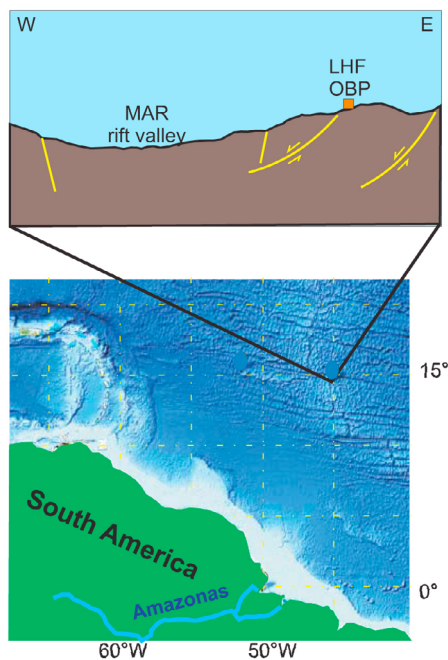


Figure 1. Geographic and tectonic location of the LHF and the OBP on a terrace at the eastern flank of the MAR (map modified from Google maps © Google Inc. Used with permission).

monitor the activity in the LHF with simultaneous monitoring of ocean bottom pressure and seafloor tilt and observations of hydrothermalism by measuring temperatures of the seafloor, bottom water and diffuse and focused hydrothermal outflows.

[8] In this paper we describe the OBPs which we developed, the measurement campaigns and data processing, discuss the results separated by their frequency content, describe the observed variations and try to analyze them in depth to determine their origins. Finally we summarize our results and present our plans for future deployments derived from our experiences in these campaigns.

2. Instrumentation

[9] Two generations of ocean bottom pressure meters (OBP1 and OBP2) were developed and constructed at the University of Bremen (Bremen, Germany). In both units, a pressure gauge, electronics and battery pack are installed in a stainless steel frame that stands on three feet to avoid wobbling. Its total weight is about 25 kg in seawater. Both instruments utilize factory calibrated quartz crystal resonators from Paroscientific Digiquartz® as pressure and temperature sensors ([\[paroscientific.com/uwapp.htm\]\(http://www.paroscientific.com/uwapp.htm\)\) with a working range from 0 Pa to 70 MPa. The product data sheet states that this pressure gauge is calibrated to an accuracy, hysteresis and repeatability of better than 0.01% full scale, i.e., 7 kPa absolute accuracy, and a resolution of \$10^{-8}\$ full scale \(0.7 Pa\). However, the two systems differ in their frequency-counting and data-handling electronics.](http://www.</p></div><div data-bbox=)

[10] OBP1 contains a Paroscientific 8CB7000-I (serial 94943) depth sensor, Pressure and temperature are calculated by the built-in electronics and digitally transmitted to a serial port. A data logger collects the data at a sampling period of 2 min with a data storage capacity of about 9 months. A separate battery package of 9 Lithium-Thionyl Chloride D cells operating at 10.8 V and 55 Ah allows slightly more than 1 year of operation with the settings of deployment 1 (Table 1).

[11] The resolution of the frequency measurements (i.e., pressure and temperature measurements) generally increases with the time span during which resonator cycles are observed, but the temporal resolution simultaneously drops. The Paroscientific pressure gauge 8CB7000-I with digital frequency output has a characteristic resolution versus integration time that allows a resolution of approximately 1 mm wce at an integration time of 4 s.

[12] The OBP2 uses a Paroscientific Digiquartz® 8B7000-2 pressure sensor. To determine the frequencies from the analog output of this gauge, a new set of counting electronics known as PPC was obtained from the manufacturer, Bennest Enterprises (Summerland, British Columbia, Canada). This period counter gives an approximately 26 times higher resolution for the same integration time compared to the native Paroscientific counter used in OBP1; thus, the instrument can employ much shorter counting time intervals and consequently gains increased temporal resolution and longer battery life. Frequencies measured with the PPC are stored by a Compact Flash data logger (built by Minerva Enterprises Ltd., Victoria, Canada) onto a 1 GB capacity Compact Flash Card. The energy is provided by a battery package (277.5 Ah @ 7.2 V) of standard Lithium-Thionyl Chloride D cells inserted into the same pressure case as the electronics; the batteries supply energy sufficient for more than 5 years of sampling temperature and pressure with a resolution of about 0.7 Pa (0.07 mm wce) at 0.5 Hz (Table 1). Systems with similar electronics were recently installed to monitor the



Table 1. Measurement Parameter for the Three Campaigns

| Deployment | Instrument | Start of Data Set | End of Data Set | Length of Data Set (days) | Sampling Period (s) | Integration Time (s) | Restorable Frequencies (Hz) | | 50% Attenuation Above (mHz) |
|------------|------------|-----------------------|-----------------------|---------------------------|---------------------|----------------------|-----------------------------|---------|-----------------------------|
| | | | | | | | Minimum | Maximum | |
| 1 | OBP1 | 22 May 2005, 21:35:10 | 10 Feb 2006, 19:03:10 | 263 | 120 | 30 s | 4.4×10^{-8} | 0.0042 | 0.02 |
| 2 | OBP2 | 28 Jan 2007, 15:59:00 | 23 Dec 2007, 21:12:00 | 329 | 2 | 1.2 s | 3.5×10^{-8} | 0.250 | 0.50 |
| 3 | OBP1 | 17 Dec 2007, 15:01:00 | 1 Feb 2009, 15:07:00 | 412 | 120 | 15 s | 2.8×10^{-8} | 0.0042 | 0.04 |

hydrological circulation in the seafloor in the framework of the Integrated Ocean Drilling Program (IODP) in the Cascadia Basin [Davis *et al.*, 2010] and in the Nankai Trough.

3. Deployment

[13] Ocean bottom pressure monitoring was conducted in three phases at the LHF. The instruments were deployed and recovered from a research vessel utilizing a remotely operated vehicle (ROV) during four different cruises between 2005 and 2009. The OBP location remained exactly the same during the whole period and was chosen by three criteria: (1) the device should be placed within the hydrothermal field to get maximum pressure signal from the underlying hydrothermal system; (2) the device should not be affected by direct hydrothermal outflow to avoid corrosion, thermal expansion and the need for extreme temperature corrections to the data; and (3) the OBP should sit on stable horizontal ground. A location was found (Figure 1) about 100 m from known hydrothermal outlets in a saddle-like structure at 14°45.2090'N, 44°58.7774'W at 3035 m water depth with minimal slope and no indications of current hydrothermal activity. Due to the lack of ship availability, the recovery of the initially deployed OBP1 was delayed by more than 1 year with a consequent data gap from 10 February 2006 to 28 January 2007. The next exchange of the instruments in December 2007 was planned in such a way that a monitoring overlap period of 6 days would allow us to compare the data and performance of both instruments.

4. Data and Processing

[14] During all three deployments with two different instruments, the OBPs worked without any problem and provided 1004 days of high-quality pressure

and temperature data (Figure 2). The measured frequencies were converted to temperature and pressure data based on the calibration function provided by the manufacturer (Paroscientific). The instrument settings (e.g., integration time and sampling rate) can be found in Table 1. A nonzero integration time interval acts as a low-pass filter with a pass function described by equation (1) with D as the frequency characteristic, $t_{\text{integration}}$ as the integration time interval and f as the observed frequency [Kiencke and Eger, 2005].

$$D(f) = \frac{\sin(t_{\text{integration}} \cdot \pi \cdot f)}{t_{\text{integration}} \cdot \pi \cdot f} \quad (1)$$

The resulting frequency characteristics of the three deployments are shown in Table 1. The fraction of these frequencies that can be reproduced correctly from the data is limited by the sampling rate, i.e., its Nyquist frequency.

[15] The chosen sampling periods result in different upper limits of the restorable frequencies at the corresponding Nyquist frequencies of 4.2 mHz and 250 mHz, respectively (Table 1). Signal frequencies in the water column above the Nyquist fre-

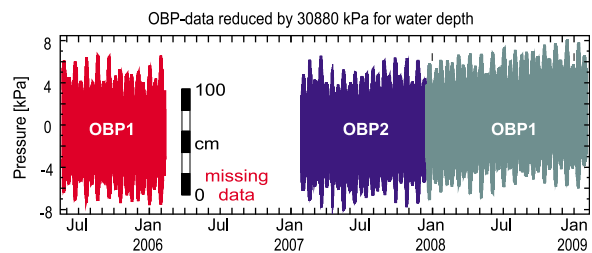


Figure 2. Complete data set of OBP measurements in the LHF between May 2005 and January 2009. The raw data were only reduced for water depth using a mean value of 30.88 MPa. Different colors indicate different measurement campaigns, and the annotation (OBP1 or OBP2) is the instrument ID.

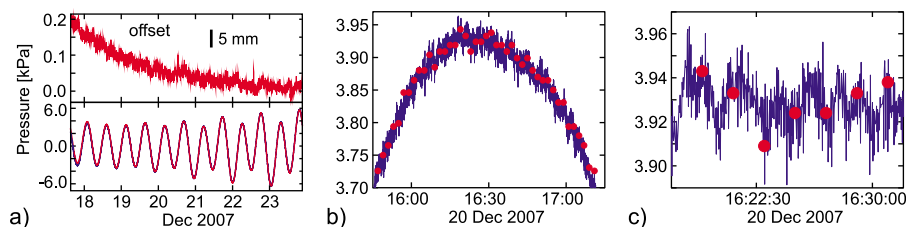


Figure 3. Comparison of OBP2 data (blue line) from the end and OBP1 data (red dots) from the beginning of their respective deployments in the time interval when both instruments were placed next to each other. The mean pressure was subtracted from both data sets. OBP2 was run at a 1.2 s integration time and a 2 s sampling period, while OBP1 was operated at a 15 s integration time and a 120 s sampling period. (a) Both data sets (lower plot) and the difference OBP1-OBP2 (upper plot) with its small initial exponential drift. (b and c) Zoom-in view of details and display of the superior temporal resolution of OBP2 compared to OBP1.

quency are attenuated due to integration time by more than 50% beyond 20 mHz, 500 mHz and 40 mHz in the three campaigns (equation (1)). The lower boundary of frequencies that can be recognized depends only on the total length of the time series [Wayne, 1987].

[16] A comparison of pressure data from 18 to 23 December 2007, when OBP1 and OBP2 were recording simultaneously next to each other, shows a small 0.2 kPa exponential initial decay of the newly deployed instrument (Figure 3a) and very good agreement between both instruments while the increased temporal and pressure resolution of OBP2 is evident (Figures 3b and 3c). The exponential decay of the offset is interpreted as instrumental drift due to the adaptation of the sensor to the high pressure of about 30.875 MPa.

[17] Because the seafloor pressure signal is dominated by the tidal signal of up to ± 7 kPa and hereby masking all small amplitude nontidal contributions, detiding of the pressure data is an essential processing step. We prefer subtraction of the modeled tides over low-pass frequency filtering because the full frequency spectrum survives in the detided data, i.e., nontidal pressure signals that occur in the frequency range of the tides are not removed. A further advantage of this technique is that filter effects are avoided. We applied the most recent tidal model TPXO.71 [Egbert and Erofeeva, 2002] using 11 tidal constituents to calculate the tidal pressure time series at the OBP location with the appropriate correction term for the depth-pressure conversion in our investigation area [Leroy and Parthiot, 1998]. The accuracy of the tidal model is on the order of 150 Pa (1.5 cm wce [Ray and Egbert, 2006]) while the precision of the depth-pressure conversion formula is known to be better than 500 Pa for all ocean depths and geographic

locations. The computed tidal pressure signal was subtracted from the original pressure data (Figure 4).

5. Discussion

[18] The detided pressure data (Figures 4a–4c) shows pressure variations with very different periods ranging from years to seconds. Long-term variations are defined as trends in the data which can be described by a superposition of an exponential and linear function. Medium-term variations have periods on the order of hours to months whereas short-term variations are pressure changes oscillating at periods of seconds to minutes.

[19] Seafloor pressure recordings represent the integrated signal of the pressure column above the instrument reaching from the seafloor up to the atmosphere. Therefore, it is very difficult to separate the different effects of tectonic, oceanographic and meteorological origin. Satellite altimetry, satellite gravity, ocean modeling and reference pressure data from a nearby location were used in an attempt to distinguish tectonic signals from all

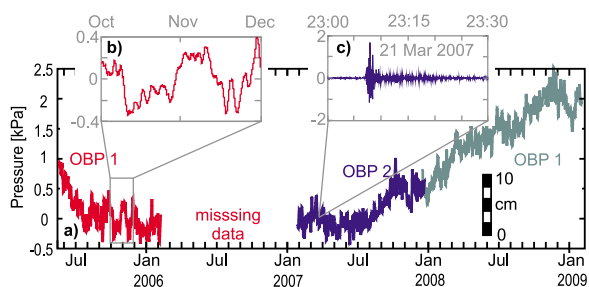


Figure 4. (a) OBP data from three OBP deployments at the LHF after subtraction of mean water depth and modeled tides. (b) Medium-term and (c) short-term pressure variations.

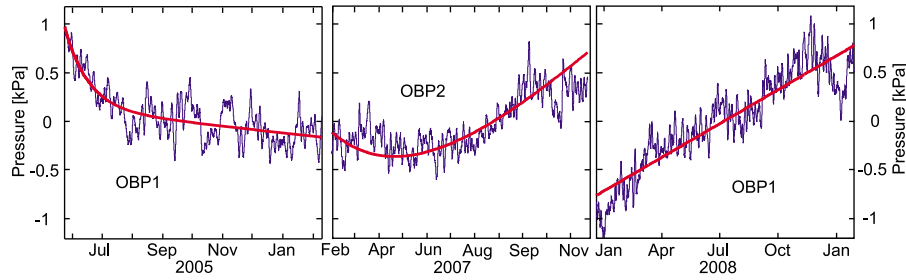


Figure 5. Individual exponential-linear fits to each OBP data set from three subsequent campaigns in the LHF.

other sources in the medium-term pressure variations. Short-term pressure changes were investigated in the context of data from weather buoys and the global teleseismic network to find possible hints to hydrothermal or volcanic activity.

5.1. Long-Term Variation

[20] An instrumental drift component is expected to be observed for each deployment of pressure sensors due to mechanical creep of the materials under high pressure [Wearn and Larson, 1982] and due to drift of the reference clock for the signal frequency measurements. The drift of pressure sensors was found to be modeled best by a combination of an exponential and a linear function (equation (2)) [Watts and Kontoyiannis, 1990] with the exponential term describing the initial adaptation of the sensor to in situ pressures and temperatures and the linear term characterizing the long-term linear drift with t as time in years and P_{drift} as pressure in kPa. The coefficients A were determined for each deployment period by a least squares fit of our 4 mHz low-pass filtered data to equation (2) (Figure 5 and Table 2).

$$P_{\text{Drift}} = A_1 \cdot e^{A_2 \cdot t} + A_3 \cdot t + A_4 \quad (2)$$

The OBP data in the first and second deployments show a pronounced exponential variation over a few months (Figure 5). In the third deployment period (2008), there is no further initial exponential decay after an initial few days, which may be due to the fact that this instrument had already been used previously for 20 months (2005/2006) at exactly the same depth as the deployment in 2007–2009. However, Polster *et al.* [2009] report in their study that sensors used

for multiple deployments showed a different drift each time that did not decrease with the number of deployments. While the first and second OBP deployments are separated by a data gap of several months, the third OBP replacement in December 2007 was accomplished with a few days of overlapping recording. The linear pressure trend at the end of the OBP2 mission in December 2007 is very similar to the purely linear trend of the subsequently deployed OBP1. It is tempting to accept this close similarity of the linear trends from consecutive deployments as an indicator of a true seafloor subsidence at 17 cm/a. However, the assumption of zero drift for both instruments cannot be verified, and the range of the linear coefficients of -0.4 to 2 kPa/a is clearly within the drift observed with Paroscientific deep sea pressure sensors [Polster *et al.*, 2009] and with -6 to 28 ppm per year is close to the median of 7 ppm, which Paroscientific observed in a long-term investigation of their barometers (<http://www.paroscientific.com/pdf/dqadavantage.pdf>). Consequently none of the observed long-term variations can be discerned from instrumental drift.

5.2. Medium-Term Variation

[21] Frequency analysis of the OBP data revealed peaks at the tidal periods as long-term, diurnal, semidiurnal, and their higher harmonics terdiurnal, quarter diurnal, and eighth diurnal. Additionally peaks at 5.0 h, 3.4 h, 2.7 h, 2.5 h and 2.1 h were found in all three data sets (Figure 6). These might reflect internal wave activity. In contrast to the observations of Fabian and Villinger [2008] and of Sohn *et al.* [2009] we did not find prominent peaks

Table 2. Linear-Exponential Approximation of the Three Data Sets From the LHF OBPs

| Deployment | Instrument | Deployment Period | A_1 (kPa) | A_2 (1/a) | A_3 (kPa/a) | A_4 (kPa) |
|------------|------------|-------------------------|-------------|-------------|---------------|-------------|
| 1 | OBP1 | 22 May 2005–10 Feb 2006 | 0.84 | -15.25 | -0.41 | +0.07 |
| 2 | OBP2 | 28 Jan 2007–23 Dec 2007 | 1.35 | -2.94 | 2.05 | -1.40 |
| 3 | OBP1 | 17 Dec 2007–1 Feb 2009 | 0 | 0 | 1.38 | -0.78 |

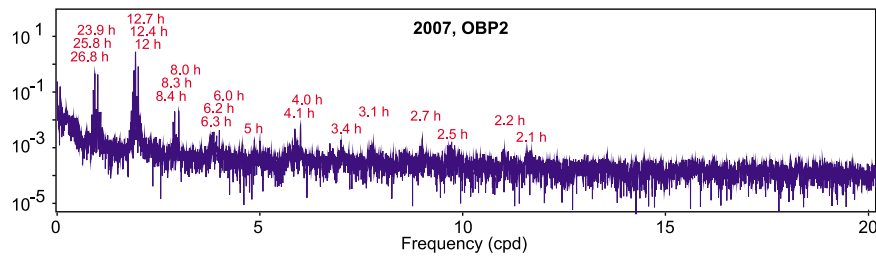


Figure 6. Spectral analysis of OBP2 data from 2007. Spectral peaks that were found also in the two other data sets were labeled. Besides the long-term, diurnal, and semidiurnal tidal periods and their higher harmonics at terdiurnal, quarter diurnal, and eighth diurnal, additional peaks were found at 5.0 h, 3.4 h, 2.7 h, 2.5 h, and 2.1 h possibly reflecting internal wave activity. No prominent peaks at periods below 2 h were found.

at periods below 2 h. *Sohn et al.* [2009] interpreted periodicities between 22 min and 53 min in his data from the TAG hydrothermal field (26°N, MAR) as caused by seafloor deformation due to subsurface pressure variation.

[22] For further investigation, a joint data set consisting of data from all three deployments was created from the detided and detrended data sets. The medium-term variations were detrended and low-pass filtered with a maximum frequency of 4 mHz (equivalent to a period of 250 s) and resampled to 120 s intervals. The resulting pressure variations (Figure 7) have peak-to-peak amplitudes of up to ± 0.7 kPa (± 7 cm wce). During the first deployment in 2005, we see a clear medium-term oscillatory component in the bottom pressure. The autocorrelation of the data (Figure 8) from 2005 reveals a period in the range of 38 days that was not detected in 2007. In 2008, a weak periodicity of about 145 days is observed, which is 4 times longer than the periodicity observed in 2005. We examined other data sets to try to explain the origin of these observations.

5.2.1. Oceanographic Situation

[23] The LHF is located below the North Equatorial Current (NEC) in the southern part of the subtropical gyre in the North Atlantic (Figure 9). This surface current is driven by the northeasterly trade winds and deflected by the Coriolis force to the right, i.e., to a more westward direction. In the context of the accompanying surface streams of the subtropical gyre like the Gulf Stream (GS), Azores Current (AC) and Canary Current (CC), Ekman transport [Steward, 2008] builds up a dome-like structure of up to 2 m of dynamic height in the center of the gyre (Aviso, time series data of Absolute Dynamic Topography Merged, 2010, <http://las.aviso.oceanobs.com/las/servlets/dataset>).

Below these surface currents, the North Atlantic Deep Water (NADW) is flowing in a southeastern direction as a part of the Meridional Overturning Current (MOC). Variations within this oceanographic setting result in a changing mass distribution and consequently in variations of the ocean bottom pressure.

5.2.2. Satellite Altimetry

[24] As bottom pressure is the integral of density multiplied by gravity from seafloor to sea surface plus the weight of the air column, the influence of sea surface height is investigated as a first step. Sea surface heights are relative to the Earth ellipsoid and a sum of the variations due to ocean currents, tides, the atmospheric loading effect and thermodynamic processes. We examined multimission (Jason-1 and -2, T/P, Envisat, GFO, ERS-1 and -2 and Geosat) derived sea surface heights available from the Aviso data center [Dibarboure et al., 2008] to show the temporal variation at the longitude of the LHF 45°W in a time-latitude diagram (Figure 10). The sea level anomalies are provided weekly by the Aviso data center on a $1/3^\circ \times 1/3^\circ$ grid and show a standard deviation of ± 4.8 cm at the LHF location (Figure 10a). As sun radiation creates steric (height variation without mass change) signals in the sea surface height mainly by

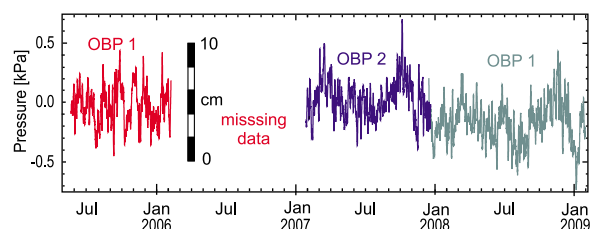


Figure 7. Residuum of the OBP data after subtraction of modeled tides, mean pressure, long-term pressure variation, and frequencies above 4 mHz.

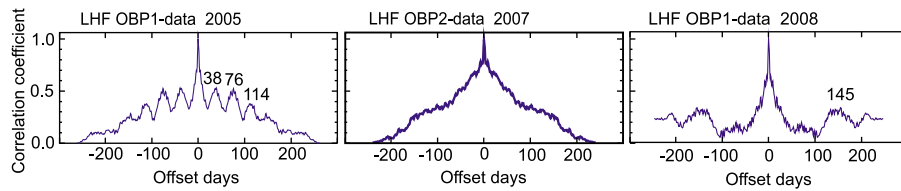


Figure 8. Autocorrelation of OBP data from the LHF. While in 2005 a clear periodicity is found, this is not the case in 2007, and only a weak 145 day periodicity is found in 2008.

thermal expansion in the ocean surface layer [Chen *et al.*, 2000] a seasonal variation depending on the solar incidence angle occurs. We calculated the zonal mean of sea level height between 30°W and 55°W to approximate this variation. A clear seasonal signal with standard deviation of ± 3 cm is evident (Figure 10b). This signal is not expected to be observed in the bottom pressure and its removal is appropriate to emphasize a bottom pressure relevant signal. The residuum sea level at LHF varies with a standard deviation of ± 2.8 cm (Figure 10c). The longitude-time diagram of the seasonal corrected sea surface heights at the latitude of the LHF (14°45'N) shows a very pronounced west trend in the relative sea surface height signals (Figure 11a). These changes can be regarded as long-wavelength waves traveling at velocities of 0.09 to 0.12 m/s, which are in the velocity range expected for the phase speed of first mode baroclinic Rossby waves at 14.75°N [Chelton and Schlax, 1996; Rossby and Collaborators, 1939]. Computing the dispersion relation for zonal propagation of baroclinic Rossby waves [Kanzow, 2004] in the Atlantic Ocean at the latitude of the LHF with coefficients for the estimation of the Rossby radius from Chelton *et al.* [1998] yields a reasonable wavelength beyond

900 km (Figure 11b). Therefore, the observed sea level variation in the satellite altimetry is interpreted to be long first-mode baroclinic Rossby waves.

[25] The comparison of the in situ bottom pressure and satellite derived sea level data (Figure 12) from the LHF does not show any correlation in shape or amplitude even after subtraction of the seasonal signal. This is obviously a large-scale phenomena as we found surface height and bottom pressure also uncorrelated at the oceanographic mooring MOVE1 installed 703 km west of the LHF (data provided by K. U. Send, Scripps Institution of Oceanography, La Jolla, United States, Figure 13) likewise reported by Bryden *et al.* [2009] from the oceanographic RAPID array more than 1000 km further north in the Atlantic Ocean at 26°N. Also our results support the conclusion from the modeling of Vinogradova *et al.* [2007] who found the sea level and bottom pressure to be increasingly uncorrelated toward lower latitudes.

[26] As baroclinity defines a system with horizontally variable densities, it is not unexpected that density variations can create a surface topography that is isostatically balanced and therefore not

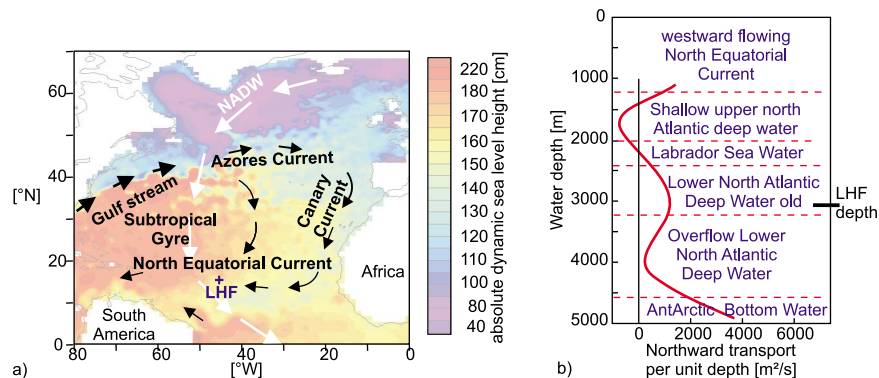


Figure 9. (a) Absolute dynamic sea level height (Aviso, time series data of Absolute Dynamic Topography Merged, 2010, <http://las.aviso.oceanobs.com/las/servlets/dataset>) in the North Atlantic overlaid by location of surface currents (black arrows), the path of the North Atlantic Deep Water (white arrows), and the location of the bottom pressure sensor in the LHF (blue cross). (b) Vertical section through water column 600 km to 1300 km west of the LHF modified after Kanzow *et al.* [2008].

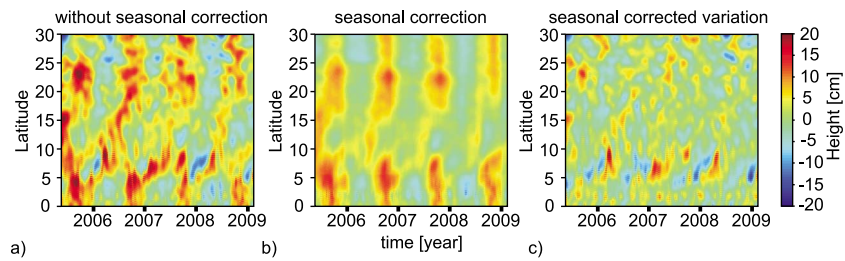


Figure 10. Latitude–time diagrams of the relative sea level in the Atlantic Ocean from satellite altimetry. (a) Sea level variation along a meridional section at 45°W. (b) Variation of the zonal mean height in the Atlantic Ocean depending on time and latitude used for seasonal correction and (c) residuum at 45°W after correction for seasonal components.

associated with a bottom pressure signal. We find the observed pressure variations at the seafloor do not reflect the westward traveling baroclinic Rossby waves; conversely, the bottom pressure variations cannot be directly derived from known sea surface heights at LHF.

5.2.3. Comparison With a Neighboring OBP

[27] While correlations do not exist between sea surface heights and measured bottom pressures, correlations between bottom pressure from two locations, MOVE1 and the LHF, reveal a remarkable coherence (Figure 13) as was previously observed with the MOVE3 mooring about 1000 km west of MOVE1 by *Kanzow et al.* [2005]. Major pressure signals show up at both locations nearly synchronously in time and amplitude.

[28] The cross correlation between both time series (Figure 14a) shows a correlation maximum of 0.87 at a retardation of 1.3 h from MOVE1 to LHF. This

indicates a westward traveling bottom pressure anomaly. The velocity of a gravity wave with a wavelength much longer than the ocean depth is calculated by the shallow water approximation (equation (3)) [Steward, 2008] with c as velocity, g as gravity and d as ocean depth.

$$c = \sqrt{g * d} \quad (3)$$

With an average ocean depth between both locations of 3750 m (2300 m to 5200 m), the expected velocity of long gravity waves is ~ 700 km/h. The distance between both OBP locations is 703 km. Thus, the travel time for long gravity waves would be expected to be 1 h. The discrepancy between the time offset derived from cross-correlation (approximately 1.3 h) and the expected time offset from theoretical calculations (1 h) might be explained by uncertainties due to a very flat shape of the coherence function between -1 h and -2 h (Figure 14b). A bias in the exact location of the maximum within the offset time between 1 h and

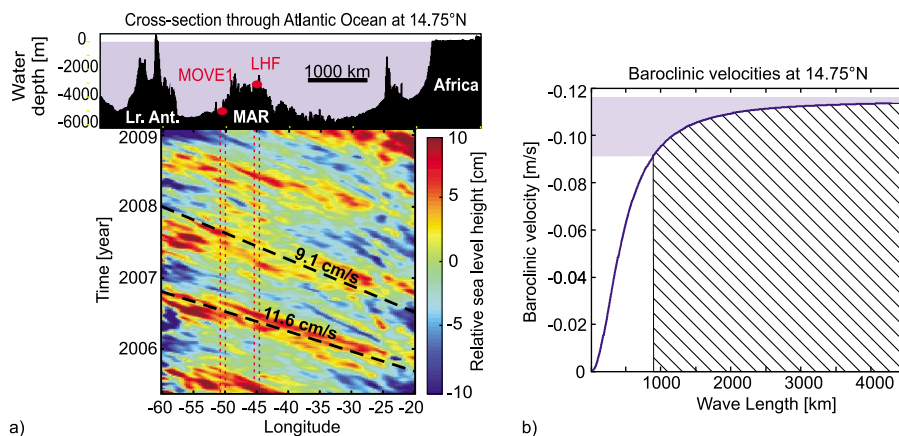


Figure 11. (a) A longitude–time diagram of relative sea height at 14.75°N from Aviso satellite altimetry after seasonal correction is shown. The locations of the oceanographic moorings for MOVE1 and the LHF are marked in the upper plot. The range of recognized west directed velocities is indicated by dashed lines of 9.1 cm/s and 11.6 cm/s. (b) Baroclinic velocities depending on wavelength and calculated from dispersion relations for zonal baroclinic Rossby waves at 14.75°N. The light blue underlying area marks the observed velocity range.

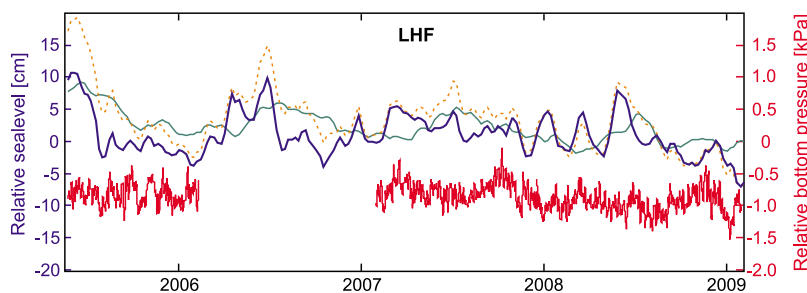


Figure 12. Time series of relative sea level at the LHF. Total variation of relative sea level (dashed orange line) derived from satellite altimetry, seasonal signal from zonal mean of sea level variation (solid green line), and the residuum after seasonal correction (solid blue line). Relative bottom pressure (solid red line) represents our in situ data from the OBP.

2 h may be due to a combination of the coarse sampling period of 10 min at MOVE1 and occasional local pressure signals that cause minor and insignificant variations in the correlation function. Propagation velocities clearly point to gravity waves as the cause for a significant part of the bottom pressure signals instead of baroclinic or barotropic Rossby waves which we attributed to the dominating waves that we observed in the satellite altimetry.

[29] Strong coherence between zonally arranged bottom pressure meters was also observed across the Atlantic Ocean at 26°N with the RAPID array.

It was interpreted as the draining and filling of the ocean in 5–10 day intervals [Bryden *et al.*, 2009].

[30] The strong coherence of pressure variations between the LHF and the MOVE array with common prominent characteristics in the range of days to weeks means that the major signals are large-scale, oceanographic effects. The offset of 1–1.5 h suggests they are dominated by gravity waves moving to the east at approximately 700 km/h. The differences between the two pressure series (Figure 13) may be associated either with local oceanographic effects or tectonic processes.

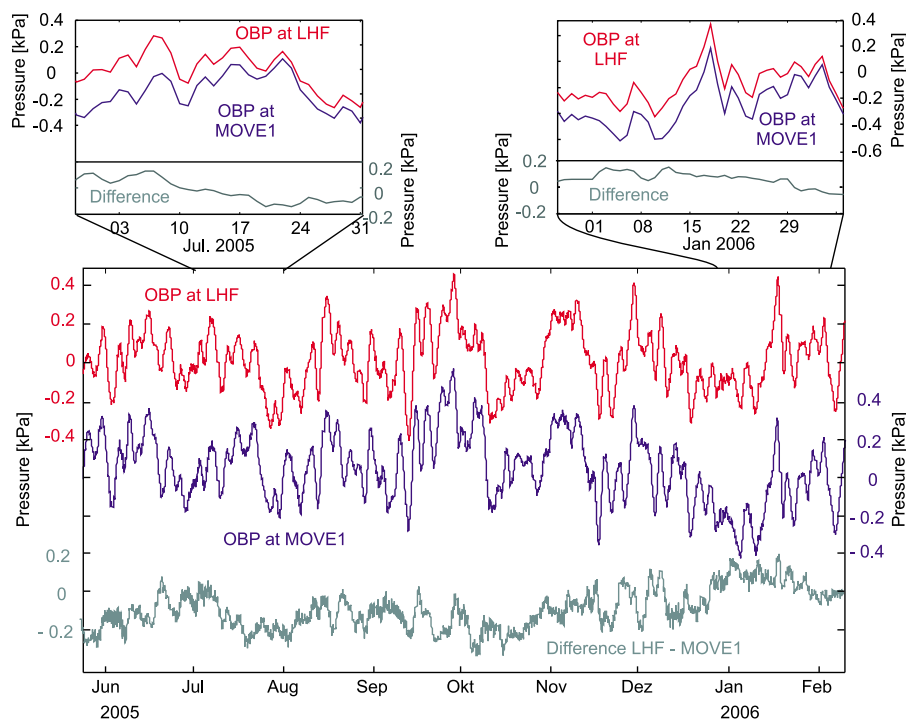


Figure 13. Comparison of OBP data from LHF (red curve) and MOVE1 (blue curve) and their difference (green curve) as overview and detail plots.

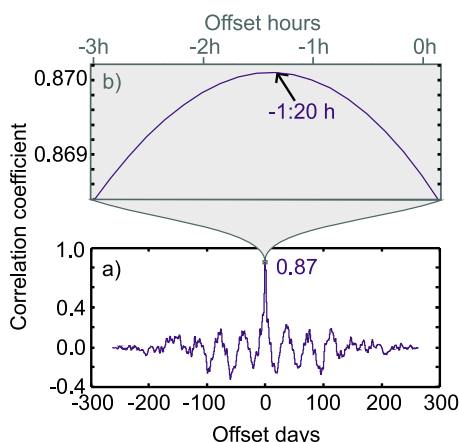


Figure 14. (a) Cross correlation between in situ bottom pressure data from the LHF and the MOVE1 location in 2005 (compare Figure 13). (b) Magnification of the central maximum of the cross correlation function.

5.2.4. Satellite Gravimetry

[31] The Earth’s gravity field is scanned in the satellite campaign of the Gravity Recovery and Climate Experiment (GRACE, <http://www.csr.utexas.edu/grace/>). Most of the monthly variations in the earth’s gravity field result from redistributions of the water masses in the oceans, land and atmosphere [Wahr *et al.*, 2004]. The advantage of gravity data over satellite altimetry is that gravity reflects the total mass distribution in the water column instead of the sea surface height; thus, the measurement also reflects density variations. The disadvantage of GRACE data is its lack of resolution due to the need of averaging in time and

space. In contrast, in situ seafloor pressure gauges measure pointwise the column mass above that instrument.

[32] We compared the solutions from the Jet Propulsion Laboratory (JPL, NASA, United States, release 4.1), GeoForschungsZentrum (GFZ, Potsdam, Germany, release 04) and Center for Space Research (CSR, University of Texas at Austin, United States, release 04) [Chambers, 2007] at smoothing radii of 300 km, 500 km and 750 km to our monthly averaged in situ OBP data. We detrended and de-meaned the GRACE data separately for the time span of each in situ OBP campaign to eliminate the effect of uncertain trends within the in situ data before we calculated the correlation coefficients. Solely the JPL solutions were partly positively correlated with our in situ data, with maximum coefficients in 2005 for the 750 km filtered, in 2007 and 2008 for the 300 km filtered GRACE solutions. Therefore we generally chose the 300 km Gaussian smoothed and destriped grid provided by JPL to compare with our in situ data (Figure 15). After subtracting the linear trends (0.74 kPa/a for the time span of the 2005 in situ data, 0.77 kPa/a for 2007 and 0.27 kPa/a for 2008) from the GRACE time series, we computed correlation coefficients of -0.50 , $+0.73$ and $+0.27$. The limited significance of a coherence analysis with detrended 8–13 months long subsets of data with a strong seasonal component (like these GRACE data) is obvious, as a significant, apparently linear, component in the GRACE subsets is neglected.

[33] A strong ambiguity within the GRACE data themselves at the LHF location becomes visible

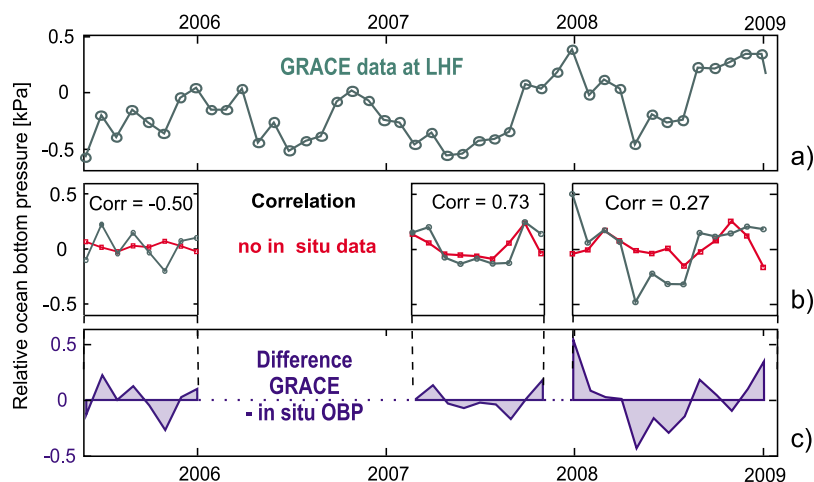


Figure 15. (a) Bottom pressure data from JPL-GRACE, Gaussian smoothed at 300 km. (b) Comparison of monthly means of in situ OBP data (red) and detrended GRACE data (green) and the respective calculated correlation coefficients “Corr.” (c) Difference between in situ bottom pressure and GRACE derived bottom pressure.



comparing the results from different processing centers. We calculated RMS differences between GFZ and JPL results of 2.3–2.7 cm water column. This matches the results of *Ponte et al.* [2007] whose global map of RMS differences between GFZ release 03 and JPL release 02 indicates the maximum of about 2–3 cm in the region of LHF.

[34] Among factors that augment the generation of artifacts in the GRACE solutions are strong signals from the periphery and high-frequency signals which are aliased. The processing centers apply different strategies like oceanic and atmospheric modeling as well as masking of problematic areas to deal with these problems thus generating different solutions. LHF and also MOVE1 are located about 1700 km north of the Amazon estuary. The very strong hydrological mass variation in the Amazon River Basin creates a gravity signal which is 10–20 times stronger than that over the ocean. This land derived signal leaks through numeric processing into the bottom pressure results from the adjacent ocean thus biasing the calculated bottom pressure results [*Böning et al.*, 2008; *Kanzow et al.*, 2005; *Rietbroek et al.*, 2006]. Filtering the GRACE data with a coherence adapted pattern filter instead of the standard Gaussian filtering improved the coherence among others at MOVE1 [*Böning et al.*, 2008]. This proves the impact of signals from the periphery at MOVE1 and probably also at LHF.

[35] Another cause for reduced coherence between the bottom pressure data from individual OBPs and GRACE RL04 results was found to be the occurrence of eddies which act only on individual OBPs [*Park et al.*, 2008]. But eddies do not seem to play a significant role at LHF as only amplitudes of about 1 cm are expected at LHF [*Chelton et al.*, 2007].

[36] For the MOVE1 location, weak correlation [*Böning et al.*, 2008] and overestimation of signal amplitudes [*Kanzow et al.*, 2005] by GRACE products were previously reported. We found the monthly averaged in situ OBP data at LHF and at MOVE1 do not show a fundamental similarity with the monthly GRACE data (Figure 15). Most signals found in the GRACE derived bottom pressure were not found within both in situ data sets, they are generally of higher amplitude and differences amount up to ± 0.5 kPa. The investigated different GRACE products differ among themselves even more at these locations. Therefore GRACE JPL 04 bottom pressures do not support us to immediately separate local tectonic effects from regional oceanographic signals at the LHF location.

5.2.5. Oceanographic Modeling

[37] Satellite altimetry and gravity data and a wealth of meteorological and oceanographic information are collected and merged into oceanic modeling by the project “Estimating the Circulation and Climate of the Ocean” (ECCO) [*Wunsch et al.*, 2009]. From among the ECCO models, we chose the JPL versions because their calculations cover the whole time span of our OBP data (Figure 15). From the five ECCO models provided by JPL (ECCO2, ECCO assimilation Kalman filtered, ECCO simulation, ECCO wind driven and OCCA), the Kalman filter controlled approach proved to be closest to our data (Figure 16). Comparing the shape of the bottom pressure curves, many signal features are found to be common in the model and our OBP data. The correlation of this model with our daily averaged in situ data is 0.7 for the 2005 data set, 0.57 for 2007 and 0.62 for 2008. Several maxima, minima and sudden pressure variations are found to be in phase and of similar shape with the in situ OBP data while the model amplitudes appear generally slightly smaller. The standard deviation of the OBP measurements is 0.17 kPa but amounts to only 0.12 kPa for the Kalman filtered ECCO model, which is an underrating by a factor of 1.4. A general underestimation of amplitudes calculated by ECCO was also reported previously by *Kanzow et al.* [2005]. The coherence between in situ measured and modeled ocean bottom pressures suggests a major part of the medium-term pressure variation is caused by oceanographic processes as modeled in the data assimilated in the ECCO project by the JPL.

5.3. Short-Term Variation

[38] In this section, we will exclusively discuss the high-frequency components of 0.04–0.250 Hz which are only contained in the 2007 OBP2 data set (Table 1). The high-pass filtered data (Figure 17b) show that the amplitude envelope of high-frequency pressure variations is variable in time. Two different characteristic features can be distinguished from the background noise. The first feature, which we call a “microseism,” gradually emerges, typically lasts for a few days, and vanishes gradually (Figure 17c). The second feature is more short-lived. It appears suddenly with nearly full amplitude, vanishes within minutes and is identified as an earthquake (Figure 17d).

[39] In calm phases, e.g., 28 May to 4 June 2007 (Figure 18a), the standard deviation of the background noise spans a range of ± 7.5 Pa. This is very

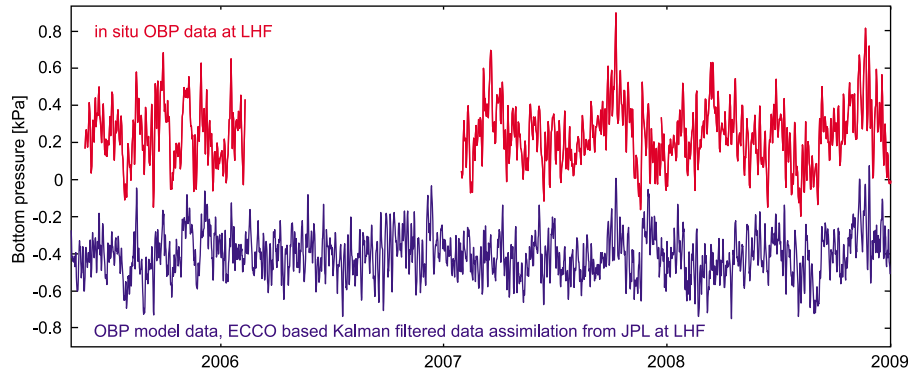


Figure 16. Comparison of in situ OBP data measured in the LHF with model data. Tides, trend, and frequencies above 4 mHz have been removed from the in situ OBP data. Model data were sampled at 12 h, Kalman filtered, and smoothed by the JPL ECCO group.

close to the noise level we found in the laboratory for the integration time that we used in the LHF deployment; thus, this lower level is defined by instrumental noise.

[40] During microseismic activity, this RMS variation typically rises for a few days, e.g., between 22 and 24 February 2007, it increases by more than a factor of 4 to ± 33 Pa (Figure 18b). The frequencies of these microseisms concentrate between 0.15 Hz and 0.21 Hz while being visible between 0.12 Hz and the recording parameter's limit of 0.25 Hz.

[41] We found that the intensity maximum in the spectrogram (Figure 19) of microseisms mimics the time series of twice the dominant frequencies from

the sea surface waves which were recorded 113 km west-southwest of the LHF location at buoy 41041 (National Data Buoy Center, <http://www.ndbc.noaa.gov/>). High amplitudes of the microseisms correspond often with high wave amplitudes and low dominant wave frequencies at buoy 41041 which suggests regional storms as a source.

[42] These results match the predictions of *Longuet-Higgins* [1950] who suggested that standing waves generated by a superposition of wave trains traveling in opposite directions such as near cyclones create microseisms through second-order pressure variations, which penetrate nearly unattenuated to the seafloor and propagate along the seafloor-water interface as Stoneley waves [*Kedar et al.*, 2008; *Longuet-Higgins*, 1950]. Therefore, the observed

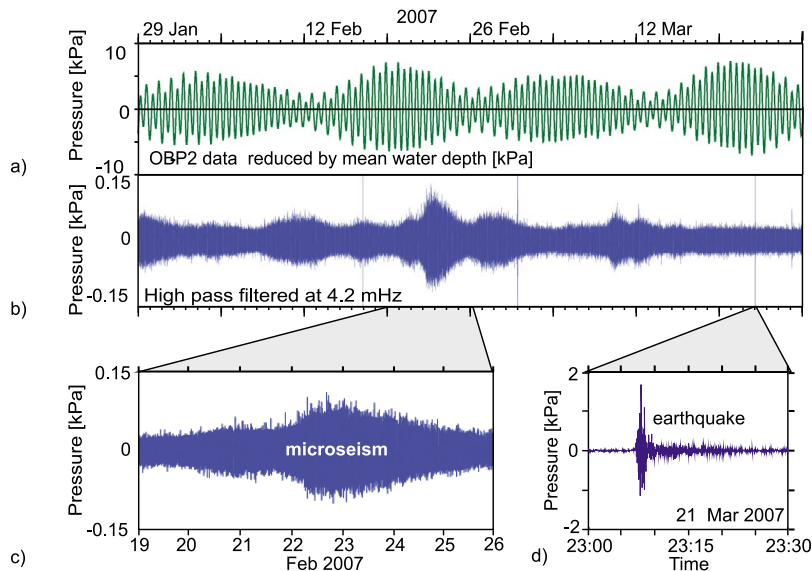


Figure 17. Examples of (a) pressure data reduced by ocean depth and (b) the residuum after detiding and application of a 4.2 mHz high-pass filter. Typical observed features in these data are (c) microseisms and (d) earthquakes.

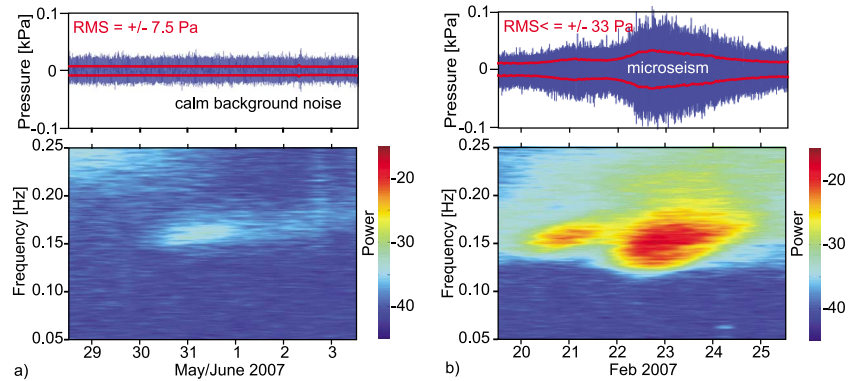


Figure 18. The high-frequency pressure variation in the top as time series and in the bottom as spectrogram. The red line in the time series plot indicates the hourly RMS amplitude during the respective intervals of (a) calm background noise with $\text{RMS} \pm 7.5 \text{ Pa}$ and (b) variation up to $\pm 33 \text{ Pa}$ during a microseism.

microseisms are not associated with subsurface magmatic or hydrothermal processes but with surface wave processes.

[43] Examining 27 earthquake-like pressure events exceeding a threshold of $\pm 0.1 \text{ kPa}$, three of these could be correlated with earthquakes large enough in amplitude to have been registered by the worldwide teleseismic network and published in the Centroid Moment Tensor (CMT) catalog [Dziewonski *et al.*, 1981]. The centroids of two shallow strike-slip earthquakes with body wave magnitudes of 5.2 and 6.3 were located at the Fifteen-Twenty and the Doldrums fracture zones in the MAR. The first occurred 21 March 2007

23:07:51 at 94 km north of the LHF (Figure 20a); the second occurred on 20 August 2007 22:42:35.5 at 968 km south of the LHF (Figure 20b). We found corresponding signals of up to 4 kPa peak to peak in the bottom pressure data at the predicted arrival times of the P_n and S_n phases, which suggests that they were converted locally into pressure waves at the seafloor/water interface. Furthermore, an earthquake of magnitude $m_b = 7.4$ was identified in the OBP2 data; it was centered 1764 km distant at a source depth of 151 km below Dominica Island in the Lesser Antilles subduction zone at 15.08°N 61.40°W on 29 November 2007 at 19:00:32.9 centroid time. Up to 1.2 kPa peak to peak pressure amplitudes occurred at the expected arrival times of

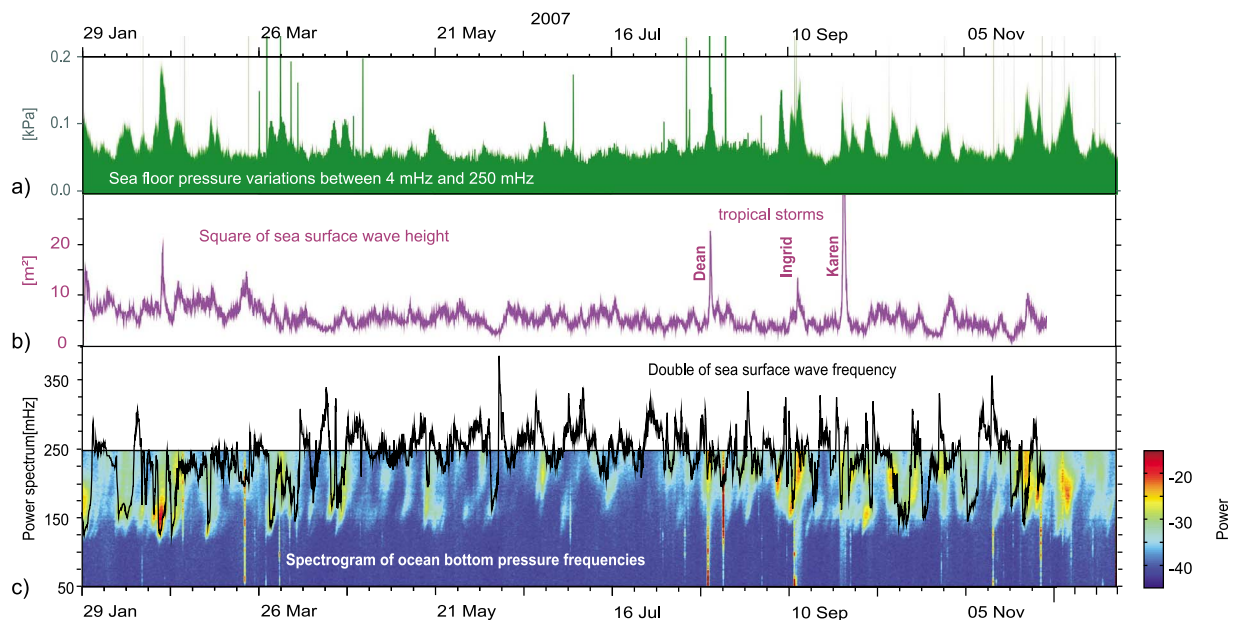


Figure 19. (a) Seafloor pressure variation, (b) surface wave height, and (c) twice the surface wave frequency (black line) overlay a spectrogram of ocean bottom pressure.

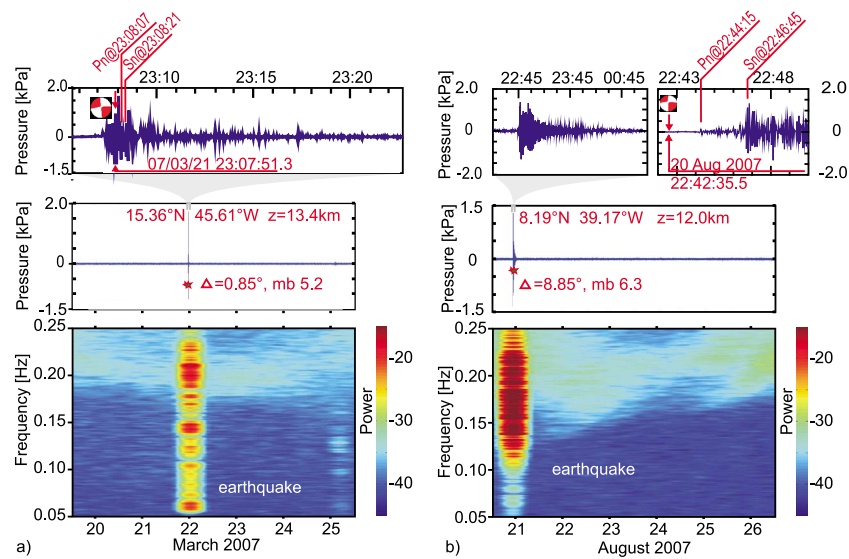


Figure 20. (a and b) The pressure signal of two seismic events registered by the global teleseismic network and published in the CMT catalog that could be assigned to strike-slip earthquakes at fault zones in the MAR. Extracts (top) from time series (middle). The corresponding power spectrograms (bottom).

the P wave and S wave from this earthquake. Because our OBPs were installed deep below the SOFAR channel [Fox *et al.*, 2001, 1995], T wave phases were not expected to be found.

6. Conclusions

[44] Two generations of OBPs were developed and constructed at the University of Bremen and were deployed in three subsequent campaigns in the years 2005 to 2009 at the seafloor in the LHF. Both instruments performed very well without failure and collected high-quality pressure data with a resolution of better than 1 mm wce.

[45] We found the linear long-term variations in OBP1 and OBP2 to be in the range of -0.4 to $+2$ kPa/a, which is always a combined effect of instrumental drift and true environmental pressure variation. All linear trends observed in our data are clearly within the amplitude range expected for drifts. Therefore, we cannot differentiate between a possible interpretation of a “breathing” hydrothermal or magmatic system below the seafloor with a sequence of subsidence and uplift by 20–30 cm on a time span of some years versus these trends explained solely by instrumental drift.

[46] We defined medium-term bottom pressure variations as the frequency interval below 4.2 mHz after the long-term variation was removed. We found tidal frequencies, their higher harmonics, and oscillations with periods of 2–5 h which possibly

reflect internal wave activity. Shorter periodicity, hinting at seafloor displacements by subsurface pressure variations, was not detected.

[47] We found that variations of the sea surface topography from satellite altimetry and ocean bottom pressure are decoupled in the LHF area. While the sea surface relief is dominated by long baroclinic Rossby waves and seasonal steric variations, neither of these was identified in our in situ ocean bottom pressure time series. Temporal changes of GRACE satellite gravity is in principle dominated by the same water redistribution processes as the in situ OBP measurements. Unfortunately, as GRACE RL04 derived variation of ocean bottom pressure from all processing centers are strongly biased by artifacts at LHF we could not utilize these data to identify regional oceanographic signals. In contrast, ECCO ocean models were positively correlated with our OBP data. Among several ECCO models, the Kalman filtered assimilation model from JPL corresponds best to our in situ data with correlation factors between 0.57 and 0.7. Even higher coherence of 0.87 with the LHF in situ OBP data was found with the in situ OBP time series from the MOVE1 mooring located 700 km to the west. In summary, we conclude that our observed medium-term pressure anomalies are dominantly large scale oceanic phenomena which travel at the speed of ocean gravity waves.

[48] In the short-term pressure variations with frequencies above 4.2 mHz, microseisms and earthquakes were recognized. The microseisms emerge



gradually, last for a few days and vanish gradually. With amplitudes of up to 33 Pa RMS they stand out from the instrumental noise floor of 7 Pa RMS. We conclude that the microseisms are caused by sea surface waves as their frequencies mimic twice the dominant sea surface wave frequencies recorded at a 113 km distant NDBC weather buoy. The earthquakes, in contrast, appear more suddenly and decay within tens of minutes. From the 27 pressure signals which we attributed to earthquakes, we assigned three with pressure amplitudes between ± 0.8 kPa and ± 2.0 kPa to teleseismic events with body wave magnitudes between 5.2 and 7.4 that were located between 94 km and 1764 km distant. We suppose that the 24 earthquake signals that could not be assigned to teleseismic earthquakes were caused by local seismic events with magnitudes too low to be registered at distant seismometers.

[49] Except the possibly local earthquakes we did not find any pressure signals from tectonic, magmatic or hydrothermal activity in the LHF, which is obviously present as focused high-temperature venting, diffuse venting and block faulting are observed at LHF. Differences between our in situ OBP data and the well correlated in situ OBP at MOVE1 or the ECCO model have low amplitude which we cannot separate from small-scale heterogeneity in the oceanography or modeling inaccuracies.

7. Outlook

[50] The apparent alternation between subsidence and uplift in the long-term trend of our OBP data would have been more convincing if a single OBP had been deployed over the whole length of the survey. For future deployments, individual bottom pressure gauges should be deployed for as long as possible. If an instrument replacement is necessary, an overlap of several months should be made to determine the individual drifts of pressure gauges to be able to separate long-term variations of the pressure from distinct instrumental drifts. The need for a pressure gauge with a more constrained long-term drift is obvious.

[51] As for medium-term variations, a 700 km distant second OBP showed extremely high coherence, and we expect that a reference station closer to the OBP would have shown even more correlation. This suggests that a reference OBP station within some kilometers from the observing OBP would be valuable to distinguish medium-term variation within the in situ bottom pressure data, which are

caused by water mass redistributions from those caused by volcanic or tectonic seafloor movements.

Acknowledgments

[52] The German National Science Foundation (DFG) funded priority program 1144 during which all three deployments of the OBPs took place. All surveys were conducted with the excellent support of the R/V *Meteor* and R/V *M.S. Merian* crews and the crews of the ROV *Quest* (MARUM, Bremen, Germany) and *Jason II* (WHOI, Woods Hole, United States). Bottom pressure data from the MOVE1 mooring were provided by K. U. Send and M. Lankhorst from SCRIPPS Institution of Oceanography, La Jolla, United States. Dimitri Menemenlis from JPL extracted bottom pressure data from the ECCO2 model for the LHF location. The ocean state estimates were provided by the ECCO Consortium for Estimating the Circulation and Climate of the Ocean funded by the National Oceanographic Partnership Program (NOPP). GRACE ocean data were processed by Don P. Chambers, were supported by the NASA MEASURES Program, and are available at <http://grace.jpl.nasa.gov>. We thank William Chadwick and two anonymous reviewers for their comments that helped to significantly improve the manuscript.

References

- Ballu, V., et al. (2009), A seafloor experiment to monitor vertical deformation at the Lucky Strike volcano, Mid-Atlantic Ridge, *J. Geod.*, 83, 147–159, doi:10.1007/s00190-008-0248-3.
- Böning, C., R. Timmermann, A. Macrandner, and J. Schröter (2008), A pattern-filtering method for the determination of ocean bottom pressure anomalies from GRACE solutions, *Geophys. Res. Lett.*, 35, L18611, doi:10.1029/2008GL034974.
- Bryden, H. L., A. Mujahid, S. A. Cunningham, and T. Kanzow (2009), Adjustment of the basin-scale circulation at 26°N to variations in Gulf Stream, deep western boundary current and Ekman transports as observed by the Rapid array, *Ocean Sci.*, 5, 421–433, doi:10.5194/os-5-421-2009.
- Carbotte, S. M., R. S. Detrick, A. Harding, J. P. Canales, J. Babcock, G. Kent, E. V. Ark, M. Nedimovic, and J. Diebold (2006), Rift topography linked to magmatism at the intermediate spreading Juan de Fuca Ridge, *Geology*, 34(3), 209–212, doi:10.1130/G21969.1.
- Chadwick, W. W., Jr., and R. W. Embley (1998), Graben formation associated with recent dike intrusions and volcanic eruptions on the mid-ocean ridge, *J. Geophys. Res.*, 103(B5), 9807–9825, doi:10.1029/97JB02485.
- Chadwick, W. W., Jr., S. L. Nooner, M. A. Zumberge, R. W. Embley, and C. G. Fox (2006), Vertical deformation monitoring at Axial Seamount since its 1998 eruption using deep-sea pressure sensors, *J. Volcanol. Geotherm. Res.*, 150, 313–327, doi:10.1016/j.jvolgeores.2005.07.006.
- Chambers, D. P. (2007), Converting release-04 gravity coefficients into maps of equivalent water thickness, report, 9 pp., Jet Propul. Lab., Pasadena, Calif.
- Chelton, D. B., and M. G. Schlax (1996), Global observations of oceanic Rossby waves, *Science*, 272, 234–238, doi:10.1126/science.272.5259.234.



- Chelton, D. B., R. A. Deszoeke, and M. G. Schlax (1998), Geographical variability of the first baroclinic Rossby radius of deformation, *J. Phys. Oceanogr.*, *28*(3), 433–460, doi:10.1175/1520-0485(1998)028<0433:GVOTFB>2.0.CO;2.
- Chelton, D. B., M. G. Schlax, R. M. Samelson, and R. A. de Szoeke (2007), Global observations of large oceanic eddies, *Geophys. Res. Lett.*, *34*, L15606, doi:10.1029/2007GL030812.
- Chen, J. L., C. K. Shum, C. R. Wilson, D. P. Chambers, and B. D. Tapley (2000), Seasonal sea level change from TOPEX/Poseidon observation and thermal contribution, *J. Geod.*, *73*(12), 638–647, doi:10.1007/s001900050002.
- Chouet, B. A. (1985), Excitation of a buried magmatic pipe: A seismic source model for volcanic tremor, *J. Geophys. Res.*, *90*(B2), 1881–1893, doi:10.1029/JB090iB02p01881.
- Chouet, B. (2003), Volcano seismology, *Pure Appl. Geophys.*, *160*(3), 739–788, doi:10.1007/PL00012556.
- Davis, E. E., M. J. Malone, and the Expedition 328 Scientists and Engineers (2010), Cascadia subduction zone ACORK observatory, *Integr. Ocean Drill. Program Prelim. Rep.*, *328*, doi:10.2204/iodp.pr.328.2010.
- Decker, R. W. (1986), Forecasting volcanic eruptions, *Annu. Rev. Earth Planet. Sci.*, *14*, 267–291, doi:10.1146/annurev.ea.14.050186.001411.
- Dibarboure, G., O. Lauret, F. Mertz, and V. Rosmorduc (2008), SSALTO/DUACS user handbook: (M)SLA and (M)ADT near-real time and delayed time products, *Rep. SALP-MU-P-EA21065-CLS*, 41 pp., Aviso, Ramonville-Saint-Agne, France.
- Dziak, R. P., and C. G. Fox (1999), The January 1998 earthquake swarm at Axial Volcano, Juan de Fuca Ridge: Hydro-acoustic evidence of seafloor volcanic activity, *Geophys. Res. Lett.*, *26*(23), 3429–3432, doi:10.1029/1999GL002332.
- Dziak, R. P., C. G. Fox, and A. E. Schreiner (1995), The June–July 1993 seismo-acoustic event at CoAxial segment, Juan de Fuca Ridge: Evidence for a lateral dike injection, *Geophys. Res. Lett.*, *22*(2), 135–138, doi:10.1029/94GL01857.
- Dziak, R. P., D. R. Bohnenstiehl, J. P. Cowen, E. T. Baker, K. H. R. J. H. Haxel, and M. J. Fowler (2002), Stirring the oceanic incubator, *Science*, *296*, 1406–1407, doi:10.1126/science.1072075.
- Dziak, R. P., D. K. Smith, D. R. Bohnenstiehl, C. G. Fox, D. Desbruyeres, H. Matsumoto, M. Tolstoy, and D. J. Fornari (2004), Evidence of a recent magma dike intrusion at the slow spreading Lucky Strike segment, Mid-Atlantic Ridge, *J. Geophys. Res.*, *109*, B12102, doi:10.1029/2004JB003141.
- Dziak, R. P., D. R. Bohnenstiehl, J. P. Cowen, E. T. Baker, K. H. Rubin, J. H. Haxel, and M. J. Fowler (2007), Rapid dike emplacement leads to eruptions and hydrothermal plume release during seafloor spreading events, *Geology*, *35*, 579–582, doi:10.1130/G23476A.1.
- Dziewonski, A. M., T.-A. Chou, and J. H. Woodhouse (1981), Determination of earthquake source parameters from waveform data for studies of global and regional seismicity, *J. Geophys. Res.*, *86*(B4), 2825–2852, doi:10.1029/JB086iB04p02825.
- Egbert, G. D., and S. Y. Erofeeva (2002), Efficient inverse modeling of barotropic ocean tides, *J. Atmos. Oceanic Technol.*, *19*(2), 183–204, doi:10.1175/1520-0426(2002)019<0183:EIMOBO>2.0.CO;2.
- Escartin, J., D. K. Smith, and M. Cannat (2003), Parallel bands of seismicity at the Mid-Atlantic Ridge, 12–14°N, *Geophys. Res. Lett.*, *30*(12), 1620, doi:10.1029/2003GL017226.
- Fabian, M., and H. Villinger (2008), Long-term tilt and acceleration data from the Logatchev hydrothermal vent field, Mid-Atlantic Ridge, measured by the Bremen ocean bottom tiltmeter, *Geochem. Geophys. Geosyst.*, *9*, Q07016, doi:10.1029/2007GC001917.
- Fox, C. G. (1990), Evidence of active ground deformation on the Mid-Ocean Ridge’ Axial Seamount, Juan de Fuca Ridge, April–June 1988, *J. Geophys. Res.*, *95*(B8), 12,813–12,822, doi:10.1029/JB095iB08p12813.
- Fox, C. G. (1993), Five years of ground deformation monitoring on Axial Seamount using a bottom pressure recorder, *Geophys. Res. Lett.*, *20*(17), 1859–1862, doi:10.1029/93GL01216.
- Fox, C. G. (1999), In situ ground deformation measurements from the summit of Axial Volcano during the 1998 volcanic episode, *Geophys. Res. Lett.*, *26*(23), 3437–3440, doi:10.1029/1999GL000491.
- Fox, C. G., W. E. Radford, R. P. Dziak, T. K. Lau, H. Matsumoto, and A. E. Schreiner (1995), Acoustic detection of a seafloor spreading episode on the Juan de Fuca Ridge using military hydrophone arrays, *Geophys. Res. Lett.*, *22*(2), 131–134, doi:10.1029/94GL02059.
- Fox, C. G., H. Matsumoto, and A. L. Tai-Kwan (2001), Monitoring Pacific Ocean seismicity from an autonomous hydrophone array, *J. Geophys. Res.*, *106*(B3), 4183–4206, doi:10.1029/2000JB900404.
- Fujimoto, H., M. Mochizuki, K. Mitsuzawa, T. Tamaki, and T. Sato (2003), Ocean bottom pressure variations in the southeastern Pacific following the 1997–98 El Niño event, *Geophys. Res. Lett.*, *30*(9), 1456, doi:10.1029/2002GL016677.
- Kanzow, T. (2004), Monitoring the integrated deep meridional flow in the tropical North Atlantic, 140 pp., Ph.D. thesis, Christian-Albrechts-Univ., Kiel, Germany.
- Kanzow, T., F. Flechtner, A. Chave, R. Schmidt, P. Schwintzer, and U. Send (2005), Seasonal variation of ocean bottom pressure derived from Gravity Recovery and Climate Experiment (GRACE): Local validation and global patterns, *J. Geophys. Res.*, *110*, C09001, doi:10.1029/2004JC002772.
- Kanzow, T., U. Send, and M. McCartney (2008), On the variability of the deep meridional transports in the tropical North Atlantic, *Deep Sea Res., Part I*, *55*(12), 1601–1623, doi:10.1016/j.dsr.2008.07.011.
- Kedar, S., M. Longuet-Higgins, F. Webb, N. Graham, R. Clayton, and C. Jones (2008), The origin of deep ocean microseisms in the North Atlantic Ocean, *Proc. R. Soc. A*, *464*, 777–793, doi:10.1098/rspa.2007.0277.
- Kiencke, U., and R. Eger (2005), Erfassung amplitudenanaloger signale, in *Messtechnik*, pp. 243–293, Springer, Berlin.
- Konstantinou, K. I., and V. Schlindwein (2002), Nature, wavefield properties and source mechanism of volcanic tremor: A review, *J. Volcanol. Geotherm. Res.*, *119*, 161–187, doi:10.1016/S0377-0273(02)00311-6.
- Leroy, C. C., and F. Parthiot (1998), Depth-pressure relationships in the oceans and seas, *J. Acoust. Soc. Am.*, *103*(3), 1346–1352, doi:10.1121/1.421275.
- Longuet-Higgins, M. S. (1950), A theory of the origin of microseisms, *Philos. Trans. R. Soc. London A*, *243*(857), 1–35, doi:10.1098/rsta.1950.0012.
- Mazarovich, A. O., and S. Y. Sokolov (2002), Hydrothermal fields in the Mid-Atlantic Ridge: Setting and prospects for further discoveries, *Russ. J. Earth Sci.*, *4*(6), 423–431, doi:10.2205/2002ES000104.
- Monigle, P. W. (2009), Seismic tremor at the 9°50’N East Pacific Rise eruption site, 62 pp., N. C. State Univ., Raleigh.



- Nooner, S. L., and W. W. Chadwick Jr. (2009), Volcanic inflation measured in the caldera of Axial Seamount: Implications for magma supply and future eruptions, *Geochem. Geophys. Geosyst.*, *10*, Q02002, doi:10.1029/2008GC002315.
- Park, J., D. R. Watts, K. A. Donohue, and S. R. Jayne (2008), A comparison of in situ bottom pressure array measurements with GRACE estimates in the Kuroshio Extension, *Geophys. Res. Lett.*, *35*, L17601, doi:10.1029/2008GL034778.
- Petersen, S., K. Kuhn, T. Kuhn, N. Augustin, R. Hékinian, L. Franz, and C. Borowski (2009), The geological setting of the ultramafic-hosted Logatchev hydrothermal field (14°45'N, Mid-Atlantic Ridge) and its influence on massive sulfide formation, *Lithos*, *112*(1–2), 40–56, doi:10.1016/j.lithos.2009.02.008.
- Phillips, K. A., C. D. Chadwell, and J. A. Hildebrand (2008), Vertical deformation measurements on the submerged south flank of Kilauea volcano, Hawaii reveal seafloor motion associated with volcanic collapse, *J. Geophys. Res.*, *113*, B05106, doi:10.1029/2007JB005124.
- Polster, A., M. Fabian, and H. Villinger (2009), Effective resolution and drift of Paroscientific pressure sensors derived from long-term seafloor measurements, *Geochem. Geophys. Geosyst.*, *10*, Q08008, doi:10.1029/2009GC002532.
- Ponte, R. M., K. J. Quinn, C. Wunsch, and P. Heimbach (2007), A comparison of model and GRACE estimates of the large-scale seasonal cycle in ocean bottom pressure, *Geophys. Res. Lett.*, *34*, L09603, doi:10.1029/2007GL029599.
- Pozgay, S. H., R. A. White, D. A. Wiens, P. J. Shore, A. W. Sauter, and J. L. Kaipat (2005), Seismicity and tilt associated with the 2003 Anatahan eruption sequence, *J. Volcanol. Geotherm. Res.*, *146*, 60–76, doi:10.1016/j.jvolgeores.2004.12.008.
- Ray, R., and G. Egbert (2006), The ebb and flow of tidal science and the impact of satellite altimetry, paper presented at 15 Years of Progress in Radar Altimetry Symposium, Eur. Space Agency, Venice, Italy.
- Rietbroek, R., P. LeGrand, B. Wouters, J.-M. Lemoine, G. Ramillien, and C. W. Hughes (2006), Comparison of in situ bottom pressure data with GRACE gravimetry in the Crozet-Kerguelen region, *Geophys. Res. Lett.*, *33*, L21601, doi:10.1029/2006GL027452.
- Rossby, C. G., and Collaborators (1939), Relations between variations in the intensity of the zonal circulation of the atmosphere and the displacements of the semi-permanent centers of action, *J. Mar. Res.*, *2*, 38–55.
- Rubin, A. M., and D. D. Pollard (1988), Dike-induced faulting in rift zones of Iceland and Afar, *Geology*, *16*, 413–417, doi:10.1130/0091-7613(1988)016<0413:DIFIRZ>2.3.CO;2.
- Smith, D. K., J. Escartín, H. Schouten, and J. R. Cann (2008), Fault rotation and core complex formation: Significant processes in seafloor formation at slow-spreading mid-ocean ridges (Mid-Atlantic Ridge, 13°–15°N), *Geochem. Geophys. Geosyst.*, *9*, Q03003, doi:10.1029/2007GC001699.
- Sohn, R. A., J. A. Hildebrand, S. C. Webb, and C. G. Fox (1995), Hydrothermal microseismicity at the megaplume site on the southern Juan de Fuca Ridge, *Bull. Seismol. Soc. Am.*, *85*(3), 775–786.
- Sohn, R. A., R. E. Thomson, A. B. Rabinovich, and S. F. Mihaly (2009), Bottom pressure signals at the TAG deep-sea hydrothermal field: Evidence for short-period, flow-induced ground deformation, *Geophys. Res. Lett.*, *36*, L19301, doi:10.1029/2009GL040006.
- Steward, R. H. (2008), *Introduction to Physical Oceanography*, 345 pp., Tex. A & M Univ., College Station.
- Vinogradova, N. T., R. M. Ponte, and D. Stammer (2007), Relation between sea level and bottom pressure and the vertical dependence of oceanic variability, *Geophys. Res. Lett.*, *34*, L03608, doi:10.1029/2006GL028588.
- Wahr, J., S. Swenson, V. Zlotnicki, and I. Velicogna (2004), Time-variable gravity from GRACE: First results, *Geophys. Res. Lett.*, *31*, L11501, doi:10.1029/2004GL019779.
- Watts, D. R., and H. Kontoyiannis (1990), Deep-ocean bottom pressure measurements, *J. Atmos. Oceanic Technol.*, *7*, 296–306, doi:10.1175/1520-0426(1990)007<0296:DOBPMD>2.0.CO;2.
- Watts, D. R., X. Qian, and K. L. Tracey (2001), Mapping abyssal current and pressure fields under the meandering Gulf Stream, *J. Atmos. Oceanic Technol.*, *18*, 1052–1067, doi:10.1175/1520-0426(2001)018<1052:MACAPP>2.0.CO;2.
- Wayne, R. P. (1987), Fourier transformed, *Chem. Br.*, *23*(5), 440–446.
- Wearn, R. B., and N. G. Larson (1982), Measurements of the sensitivities and drift of Digiquartz pressure sensors, *Deep Sea Res., Part A*, *29*, 111–134, doi:10.1016/0198-0149(82)90064-4.
- Williams, C. M., R. A. Stephen, and D. K. Smith (2006), Hydroacoustic events located at the intersection of the Atlantis (30°N) and Kane (23°40'N) transform faults with the Mid-Atlantic Ridge, *Geochem. Geophys. Geosyst.*, *7*, Q06015, doi:10.1029/2005GC001127.
- Wunsch, C., P. Heimbach, R. M. Ponte, and I. Fukumori (2009), The global general circulation of the ocean estimated by the ECCO-Consortium, *Oceanography*, *22*, 88–103.